International Journal of Forestry and Horticulture (IJFH)
Volume 10, Issue 1, 2024, PP 20-30
ISSN No. (Online) 2454–9487
DOI: https://doi.org/10.20431/2454-9487.1001004
www.arcjournals.org

Applying Unoccupied Aircraft System Multispectral Remote Sensing to Examine Blight in a Pacific Madrone Orchard

Michael G. Wing*, Matthew I. Barker

Department of Forest Engineering, Resources, and Management, Oregon State University, Peavy Hall, 3100 SW Jefferson Way, Corvallis, OR 97333, USA

Corresponding Author:** ***Michael Wing, *Department of Forest Engineering, Resources, and Management, Oregon State University, Peavy Hall, 3100 SW Jefferson Way, Corvallis, OR 97333, USA*

Abstract

Pacific madrone is susceptible to disease and blight from a variety of sources. Blight is a discoloration and withering of leaves that can be visually detected. Determining the cause of blight requires greater investigation and possibly lab-based testing. Our objectives were to explore the use of a multispectral sensor mounted on an unoccupied aircraft system (UAS) for investigating blight spatial-temporal patterns on individual madrone trees. We combined in situ blight detection survey methods on individual trees with UAS multi-spectral imagery collected during October of four consecutive years, and May of two consecutive years. We assessed potential relationships of blight presence with remotely-sensed vegetation health indices. We also examined potential hydrological vectors for blight patterns by investigating whether three GIS-derived water flow accumulation models were related to blight patterns. We found that the Green Red Vegetation Index (GRVI) had the strongest correlation across time with blight presence although several other indices were correlated but less consistently. We also found that the D8 flow accumulation model (Jenson & Dominque 1988) was the only model of statistical significance in determining a relationship to blight presence.

1. INTRODUCTION

1.1. Pacific Madrone Background

Pacific madrone (*Arbutus menziesii*) is a species of hardwood native to the western USA and has been waning due to the increasing fungal pathogens, including *Phacidiopycnis washingtonensis,* that promote Pacific madrone leaf blight (PMLB) (Elliott 1999; Sikdar et al. 2019). PMLB stresses leaves and makes trees more susceptible to deadly canker diseases such as *Fusicoccum spp.* (Elliott et al. 2002). It is predicted that some madrone populations may decline or disappear due to changing temperatures and precipitation associated with climate change (Elliott et al. 2012). Pacific madrone is visually distinctive by its burnt-orange bark hue that eventually lifts to uncover a light green and smooth bole. Pacific madrone reaches from southern California to Vancouver, B.C., and exists west of the Cascade Range in Oregon, USA. Madrone provides habitat for cavity nesters including woodpeckers and wrens (Reeves 2007) and produces sprouts that are browsed by sheep, goats, and deer. Madrone also produces berries that deer and many bird species feed upon (Sampson & Jesperson 1963). Madrone maintains leaves throughout the year and produces new leaf growth during spring. Madrone produces bright red berries and light-colored flowers which grow at the ends of its branches. Commercial applications include veneers, flooring, and other aesthetic uses (USDA 2006). Madrone is also planted for erosion control and as an attraction in landscaping. Madrone is capable of growing in open sites that are well-drained with rocky soils (Bennett & Shaw 2008).

1.2. Foliar Blight

Elliott et al. (2012) identified blight as a leading factor in the widespread decline of Pacific madrone. Numerous fungal pathogens can colonize young leaves and spread via spores in air or water primarily during spring rains (Bennett & Shaw 2008). Pacific madrone fungi are visible in the form of discoloration, spots, and galls on foliage. Disease can foster a tree's susceptibility to increasing fungi colonization. Maloney et al. (2004) found that infection of *A. menziesii* by the pathogenic fungus *Phytophthora ramorum with a* secondary infection by *Botryosphaeria dothidea* created greater mortality than infection by either species alone. Bennett & Shaw (2008) reported that Pacific madrone

is sensitive to foliage diseases caused by fungal organisms, that can be transported via airborne or water-splashed spores during wet weather. Foliage diseases can often lead to leaf spots that can create foliage blight and kill entire leaves. Overall madrone health is heightened through sporadic deep watering rather than frequent light watering. Root diseases can also increase foliage loss or curl and are present in moist soil conditions that are associated with overwatered, heavy clay, or poorly drained soils. Extended periods of drought can increase disease susceptibility in trees although madrones are relatively drought tolerant. Detection and management of PMLB has frequently relied on visually-based field surveys on an individual tree basis. Impacted foliage is raked and destroyed in an attempt to fortify madrone populations as blight-impacted individuals are more susceptible to severe disease and stress associated with climate change (Bennett & Shaw 2008; Elliott et al. 2012). Traditional field-centric PMLB surveys are costly due individual tree surveys and the time and expense associated with accessing stand locations which can sometimes be remote. Individual tree surveys are key in traditional PMLB assessment in leading trees managers to decide where leaf raking and burning efforts, or other activities, should occur in order to control disease spread (Bennett & Shaw 2008). Field surveys also provide a potential vector for disease spread as surveyors move through infected stands (Lucas & Dickinson 1998). Unoccupied aircraft systems (UAS) and their ability to capture high resolution imagery for remotely sensing environmental phenomena can lead to increased PMLB survey efficiency. Individual tree assessments on a stand level with a UAS can also lessen the risk of exacerbating PMLB spread through anthropogenic vectors. Our objectives were to explore the use of a multispectral sensor mounted on a UAS for investigating PMLB spatial-temporal patterns on an individual tree basis. Our approach combined in situ blight detection survey methods with UAS multi-spectral imagery collected during October of four consecutive years. We examined potential relationships of PMLB presence with remotely-sensed indices for determining vegetative health. We also investigated potential vectors for blight patterns by examining whether GIS-derived water flow accumulations were related to blight patterns.

1.3. Pertinent Previous Findings

UAS are becoming prevalent in environmental monitoring applications due to their multiple advantages over traditional field surveys and occupied aircraft remote sensing. UAS are capable of rapidly surveying modestly-sized areas in a short time are much less expensive than occupied aircraft. Guimarães et al. (2020) found that UAS remote sensing resulted in efficient forest inventory data acquisition at reduced costs and more detail than ground-based inventories. UAS remotely sensed products can characterize tree physical attributes through elevation models, ortho-imagery, and point clouds. Vegetation indices, which can be used to infer vegetative health, can also be created through combinations of spectral signatures. Vertical takeoff and landing (VTOL) vehicles with color (red, green, and blue) wavelength (RGB)) sensors are the most affordable and common in forest health monitoring for disease detection. Repeated UAS remote sensing surveys have supported multi-temporal change detection. Marques et al. (2019) demonstrated how to extract features from UAS-derived color-infrared (CIR) and true-color orthoimagery with a 16 cm ground sampling distance (GSD) to conduct a multitemporal analysis of chestnut trees. They reported a 98% success in detecting individual chestnut trees. A strong relationship between ground observations and UAS-derived tree height and diameter of R^2 correlation coefficients (0.79 and 0.92, respectively) indicated that UAS biophysical attribute estimates could support individual tree change over time. Barker et al. (2023) used a UAS to image a Pacific madrone stand and analyzed imagery using machine learning modeling. The final model detected PMLB blight status of 29 field surveyed madrone trees with a kappa coefficient of 0.71, a balanced accuracy of 0.85, and a true positive rate of 0.92. Disease presence inference has been derived by extracting physiologically relevant vegetation indices (VIs) from remotely sensed data. Marin et al. (2018) found vegetation indices derived from the Landsat 8 Operational Land Imager and Thermal Infrared Sensor were highly correlated with disease presence in the bacterial blight of coffee ($r = 0.76$) and disease severity ($r = 0.52$). Calderón et al. (2013) employed VIs to classify disease severity of *Verticillium* wilt at various stages in olive trees with high resolution UAS data. Zarco-Tejada et al. (2012) determined that water stress detection in a heterogeneous canopy within a citrus orchard was feasible with thermal and hyperspectral UAS imagery. The hyperspectral imagery was used to derive narrow-band indices that were found to be useful in stress detection. Di Nisio et al. (2020) studied 71 olive trees infected with olive quick decline syndrome through a combination of multispectral and high-resolution visible sensors. RGB, CIR, and NDVI indices were derived from UAS imagery and a Sørensen-Dice similarity coefficient that was created for each olive tree following tree segmentation.

Sørsensen-Dice coefficients were high, demonstrating successful tree delineation. Di Nisio et al. (2020) noted that NDVI alone was not sufficient for distinguishing healthy trees from healthy grass and used machine-learning techniques to assist in this distinction. The olive quick decline syndrome classifier performed well with 98% sensitivity and 100% specificity. Garza et al. (2020) determined that the correlation between a triangular greenness index (TGI) created from UAS-derived imagery and field health measurements of citrus trees were useful to assess tree health and disease status. UAS imagery has also been used in previous studies to detect blight within a variety of species. Bagheri (2020) employed a UAS equipped with a multispectral sensor to quantify fire blight in 75 pear trees affected with differing levels of disease and achieved classification accuracies for healthy, asymptomatic, and symptomatic trees of 98.7%, 91.4%, and 93.9%, respectively. Sandino et al. (2018) used hyperspectral imagery captured by a UAS and machine learning to classify myrtle rust presence in paperbark trees and determined detection rates of 97.24% for healthy trees and 94.72% for affected trees.

2. Materials And Methods

2.1. Site and Data Acquisition

The study area containing Pacific madrones is a common garden study with the aim to gather data regarding genetic traits of 105 pacific madrone families from 7 different ecoregions.

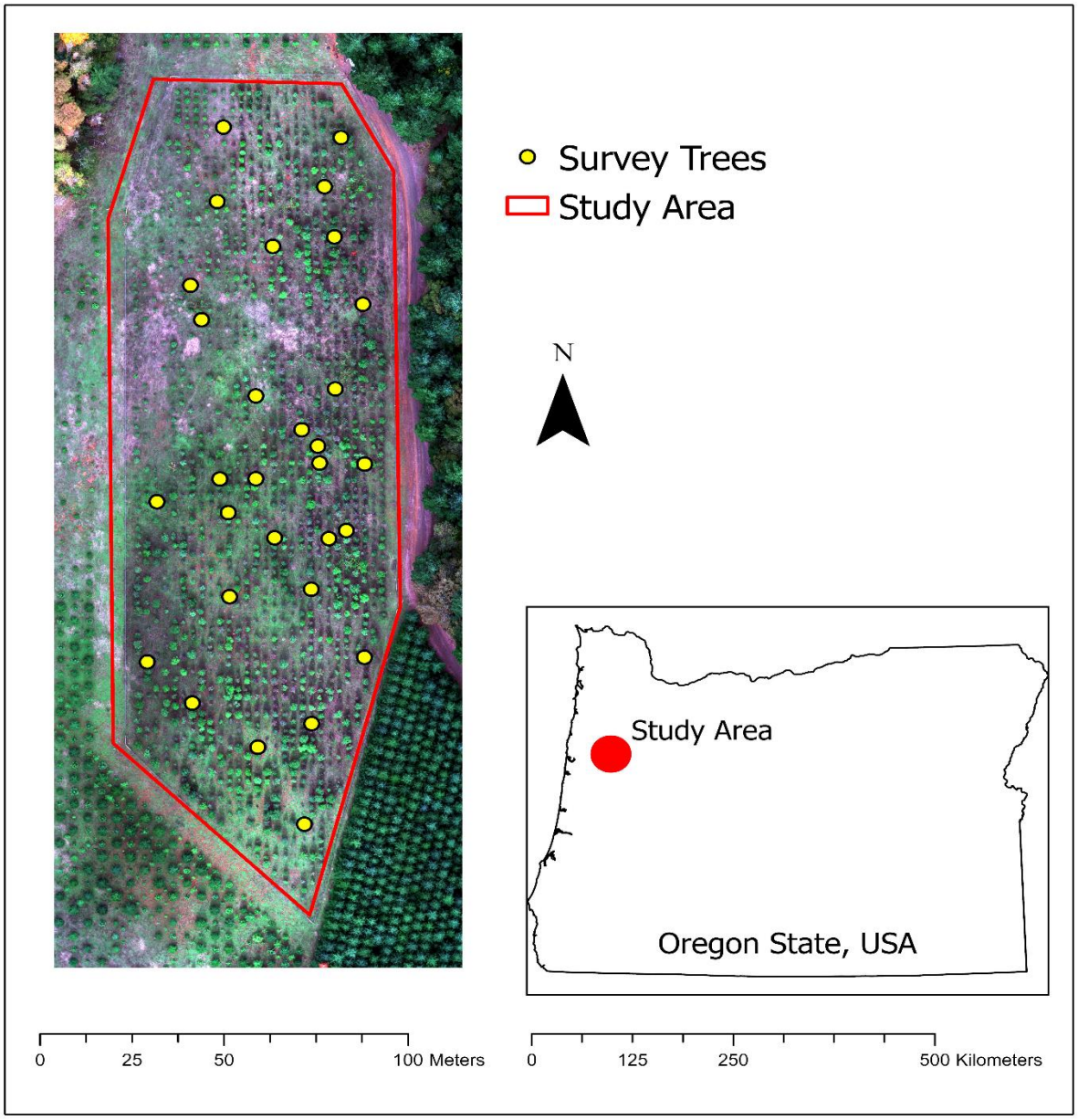

Figure 1. *Pacific madrone study site in northwest Oregon, USA. Points are locations of 29 field validation trees. Background is orthomosaic from UAS imagery flown in Oct. 2019.*

The seed for this study was collected by Washington State University from 2006 to 2010. In February of 2011, researchers sowed plug trays and moved them into a greenhouse in April of 2011. In June of 2011, seeds were germinated and placed outside until they were transplanted in the fall and winter of 2011. The genetic traits investigated included disease resistance, growth traits, and suitability to predicted conditions under climate change conditions (Eliott et al. 2012). The site is located on privately owned land located north of Corvallis, Oregon, USA near N 44°43', W 123°23' (Figure 1). The study site is approximately 1.5 ha (3.6 acres) in area with a modest elevation gradient ranging between 235 and 247 m. According to precipitation data acquired from PRISM Climate Group (2022), annual precipitation in the area was 1187 mm, 1411 mm, and 1585 mm, 1470 mm for 2019, 2020, 2021, and 2022 respectively. We conducted field and aerial surveys during six site visits occurring on October 15, 2019, May 28, 2020, October 15, 2020, May 28, 2021, October 15, 2021, and October 13, 2022 between approximately 12:00 and 15:00 PDT. The October 2019 flights occurred during scattered cloud conditions, and the May 2020, October 2020, May 2021, October 2021, and October 2022 flights during clear skies.

2.2. Ground Survey

For field validation purposes, we selected and surveyed 30 trees (ground survey trees) to characterize blight impacted to individual trees. However, one survey tree was uprooted during a wind storm in January 2021, reducing our sample size to 29. During each site visit, we revisited the same 29 ground survey trees. These trees were selected because they represented a broad spatial distribution and beset the full range of visible signs of disease, ranging from few visible signs to many affected leaves. Ground survey trees were stem mapped and georeferenced with a Trimble Geo XH global navigation satellite system receiver paired with a range pole-mounted external Tornado antenna. In each site visit, we assessed blight and measured the height of each ground survey tree. Tree height was measured with a measurement pole from base of stem to the highest point of each tree. Blight assessment was followed from methods outlined in DeWald et al. (2018) as follows: (1) Identify the most severely impacted leaf from current season growth and classify severity according to percentage of leaf area (0%, <25%, 25%-50%, >50%) exhibiting signs of blight. (2) Estimate incidence by visually examining the entire crown and estimating the percentage of tree leaves affected (<25, 25-50, 51-75, >75) by the most severe rating identified in step 1 (DeWald et al. 2018). (3) The incidence data is then used to assign a dominant severity class to each surveyed tree, and when two equally dominant severity classes are apparent, the most severe class is reported. As a result of all ground survey trees having a visual severity rating that was greater than 50%, we modified DeWald et al.'s (2018) methods to increase levels of gradation to better correspond with the extended response of indicator variables in our remotely sensed data. In our survey, we integrated current year incidence to provide a better distinction between blight impacts of the previous years. This helps account for the unbalanced large influence the leaves from the most recent growing year have on the remotely sensed signal relative to the proportion to total leaf area. The most recent growing year's leaves represent the largest proportion of the visible crown when viewed from above at nadir.

2.3. Calculating Blight Index

We produced a combined blight index based on previous work by the assessment outlined by DeWald et al. (2018). Using percent of crown impacted (incidence, ranging from 0-100) at each blight severity category: 0%, <25%, 25%-50%, >50%, we multiplied crown percentages by 0, 0.33, 0.66, and 1, respectively. Last, we calculated the sum of those four values to report a combined blight index for each ground surveyed tree that ranged from 0 – 100.

2.4. Aerial Survey

Remotely sensed imagery was collected using a Micasense Altum multispectral camera (Micasense 2020) onboard a DJI Matrice 200 v2 quadcopter UAS for flights conducted on October 15, 2019, May 28, 2020, October 15, 2020, May 28, 2021, and October 15, 2021. A DJI Matrice 300 quadcopter was used on October 13, 2022. The Altum camera contains five electrooptical (EO) bands sensitive to red, green, blue, near infrared, red edge, and one band that records radiant temperature in the longwave infrared (thermal) regions of the electromagnetic spectrum. The resolution of the EO bands and LWIR band is 4.3 cm and 67.8 cm ground sampling distance (GSD), respectively, at 100 m above ground level

for the first five bands and thermal band. Comprehensive Matrice and Altum flight and imaging specifications are described by Wing (2019). DJI Pilot Software (Year) was used to conduct flights autonomously to ensure the necessary image forward overlap and side overlap were achieved. Each flight lasted approximately 8 minutes in duration. The flight planning software allows the user to specify flight area, velocity, overlap, and altitude. The same flight plan was used for all 6 flights which included: flight altitude set to 100 m above ground level, ground velocity set to 5 m/s, forward and side overlap set to 80%. This amount of forward and side overlap produces the most geometrically accurate orthomosaics (Hostens et al. 2022; Nesbit & Hugenholtz 2019) at 25 overlapping images of any given location. Before and after each flight, we imaged a spectral calibration target with the multispectral camera to calibrate the EO bands. This step facilitates comparison of at-sensor reflectance data captured during different flights by accounting for scene irradiance and correcting using the empirical line method in photogrammetry software.

2.5. Image Processing

Using Agisoft Metashape (2024) photogrammetry software, image processing was completed with processing parameters based on sensor manufacturer's recommendations. Radiometric calibration was applied to imagery during processing in Metashape by sourcing the spectral calibration target images taking during each flight and specifying the manufacturer-provided albedo values. The five non thermal bands were transformed to from 16-bit digital numbers to surface reflectance values between 0.0 and 1.0, where 1 represents 100% reflectance of incident light for the specified band. Thermal values were converted from centi-Kelvin to Celsius (cK/100-273.15) for more direct interpretation. The subsequent orthomosaic raster files containing 6 bands had a resolution of approximately 5 cm ground sampling distance (GSD). Using the nearest neighbor assignment method, the thermal band was automatically resampled from 67.8 cm GSD to match the GSD of the non-thermal bands.

In order to produce nine vegetation indexes, the orthomosaics were imported to R (R Core Team 2021) using the Raster package (Hijmans 2018). The vegetation indexes are known to indicate the structural and/or physiological condition of vegetation (Table 1). This brought our total number of bands to 15.

Table 1. *Vegetation indices (VIs) constructed from individual bands 1-6. Reference denotes the source of the VI when applicable.*

Band	Name or Vegetation Index	Reference
1	Blue ( )	NA
2	Green ( )	NA
3	Red ( )	NA
4	Red edge ( )	NA
5	Near infrared ( )	NA
6	Longwave infrared (LWIR)	NA
7	Triangular Greenness Index (TGI)	(Hunt et al. (2011, 2013))
8	Green Red Vegetation Index (GRVI)	Tucker (1979)
9	Normalized Difference Vegetation Index (NDVI)	Rouse et al. (1974)
10	Normalized Difference Red Edge (NDRE)	Barnes et al. (2000)
11	Green Normalized Difference Vegetation Index (GNDVI)	Gitelson et al. (1996)
12	Modified Simple Ratio Index (MSR)	Chen (1996)
13	Modified Simple Ratio Index Red Edge (MSRE)	Cao et al. (2013)
14	Green Chlorophyll Index (GCI)	Gitelson et al. (2005)
15	Red Edge Chlorophyll Index (RECI)	Gitelson et al. (2005)

2.6. Tree Crown Delineation and VI Creation

To manually delineate 1,349 tree crowns, we used ArcGIS Pro Version 2.8.3 (ESRI 2024) and generated circular buffers. Circle radius and center were identified and manually measured for each tree using the true color orthomosaic from October 2019 as a reference. Using ArcGIS, the 29 ground survey trees were associated with their corresponding tree crown using GPS. Tree crown circles were exported into the R environment and using the exactextractr tool (Baston 2021), we were able to calculate the mean of each of the 15 bands (Table 1) in each of the given time periods.

2.7. Deriving Flow Accumulation from DTM

To produce a flow accumulation raster, elevation data of the AOI is required. The Oregon Department of Geology and Mineral Industries (DOGAMI) Oregon Lidar Consortium (2024) funded an aerial lidar survey mission that covered the Madrone Research Plot on 1/30/2012, reporting an RSME of 0.05m. Derived from this survey, DOGAMI Data Lidar Web Service offers a bare earth digital elevation model (DEM) data product, with spatial resolution of 3 international feet. We acquired the DEM and imported it into ESRI's ArcGIS Pro software (ESRI 2024) to convert the unit values to meters, reproject into NAD 1983 UTM Zone 10N reference frame, and clip the elevation model to the extent of the research plot boundaries. The clipped DEM raster was processed through three separate flow direction models; D8, DINF and MFD. Within ArcGIS Pro, the Flow Direction tool allows for direction of flow to be determined throughout each cell of a surface model raster through the use of one of these model algorithms. The first of these models, the D8 or eight-direction flow model (Jenson & Dominque 1988) calculates the direction of flow by determining the direction of steepest descent, effectively taking a central raster cell of highest elevation value and comparing the change in elevation between eight surrounding cells to determine the highest chance of flow based on the greatest change in elevation. An alternative method, D-Infinity (DINF) presented by Tarboton (Tarboton, 1997) determines the flow direction based on the steepest slope of a triangular facet in which flow direction is mapped from a floating point in the direction of a single angle ranging from 0 to 360 degrees counter-clockwise. The final flow direction algorithm, the Multiple Flow Direction (MFD) algorithm described by Qin et al. (2007), partitions the flow from a central raster cell across all downslope neighbors based on a function of the maximum slope gradient. This model allows for the consideration of local terrain conditions observed within the broader area of interest.

2.8. Analysis of Surface Flow on PMLB

To assess the potential impact of surface flow on PMLB prevalence, we examined statistical relationships between flow accumulation and blight index for 29 ground survey trees by producing simple linear regression models at each time step. We hypothesized trees that experience higher flow accumulation would demonstrate higher levels of blight as pathogens that cause the disease are thought to spread via water particles. Additionally, we investigated the relationship between blight index and the six bands and derived VIs to determine which variable is best suited for indicating blight. We examined Pearson's correlation coefficients via correlation matrices to assess potential relationships and produced simple linear regression models for variables with a high correlation to blight index. Following the creation of three distinct flow direction models based on the D8, DINF and MFD algorithms, the ArcGIS Pro Flow Accumulation tool was used to map the calculated accumulated weight of all cells flowing into each adjacent downslope cell in three separate flow accumulation raster models based on the initial flow direction model used. This resulted in raster models with cells that had a value based on the number of cells that flowed into each of them in the corresponding direction flow model. Having created a flow accumulation raster for each flow direction model, statistics could be calculated between the cell values of a given flow accumulation model and previously created tree canopy polygon model for the stand. In this case, a resulting table was created for each flow model in which the mean number of cells flowing into each tree canopy basal area was computed. These ArcGIS Pro tables were then exported into CSV files for further analysis.

3. RESULTS

3.1. Surveyed Trees Vegetation Index Correlations

We performed correlation calculations for the VIs and field assessed blight conditions of the 29 survey trees in the madrone stand across six remote sensing flights (Table 2). Generally, the indices were more highly correlated in the October 2019 and October 2020 site visits than the other four survey periods. The strongest correlations overall were detected in the October 2019 data with four indices (GRVI, MSR, NDVI, and TGI) having correlation coefficients greater than 0.50. The GRVI and MSR indices had correlation coefficients at or over 0.70 during this season. The GRVI index had the strongest relationship to field blight assessments in the October 2019 and May 2020 and 2021 field seasons. GRVI also had one of the stronger correlations during the October 2020 season.

Table 2. *Vegetation indices and correlations with significance levels to field assessed blight conditions for 29 survey trees. Bold font indicates significance at 0.05 p-value level.*

	Date	10/15/2019	10/15/2020	10/15/2021	10/13/2022	5/28/2020	5/28/2021
GCI	r^2	0.11	**0.23**	0.05	**0.14**	0	0
	p-value	0.08	0.01	0.23	0.05	0.86	0.95
GRVI	r^2	**0.78**	**0.33**	**0.02**	0.06	**0.43**	**0.29**
	p-value	0.00	0.00	0.00	0.00	0.00	0.00
GNDVI	r^2	**0.16**	**0.23**	0.06	0.12	0.00	0.00
	p-value	0.03	0.01	0.22	0.07	0.75	0.99
MSR	r^2	**0.70**	**0.36**	0.05	0.10	**0.25**	**0.15**
	p-value	0.00	0.00	0.24	0.10	0.01	0.04
MSRE	r^2	**0.18**	**0.35**	0.09	0.13	0.02	0.02
	p-value	0.02	0.00	0.12	0.06	0.48	0.44
NDVI	r^2	**0.60**	**0.30**	0.03	0.10	**0.27**	**0.18**
	p-value	0.00	0.00	0.35	0.09	0.00	0.02
NDRE	r^2	**0.19**	**0.36**	0.09	0.13	0.02	0.02
	p-value	0.02	0.00	0.12	0.06	0.49	0.45
RECI	r^2	**0.18**	**0.35**	0.09	0.13	0.02	0.02
	p-value	0.02	0.00	0.12	0.06	0.47	0.44
TGI	r^2	0.54	0.00	0.02	0.01	**0.22**	**0.2**
	p-value	0.00	0.72	0.51	0.56	0.01	0.02

Overall correlations between VIs and field blight assessments were the weakest during the October 2021 and 2022 seasons. The highest correlation was 0.09 (MSRE, NDRE, and RECI) during the October 2021 season and 0.14 (GCI) during the October 2022 season.

Results of multiple linear regression indicate a significant correlation between individual flight date taken as a factor along with GRVI and blight index ($p < 0.005$, adj R2 -> r^2) (Figure 2).

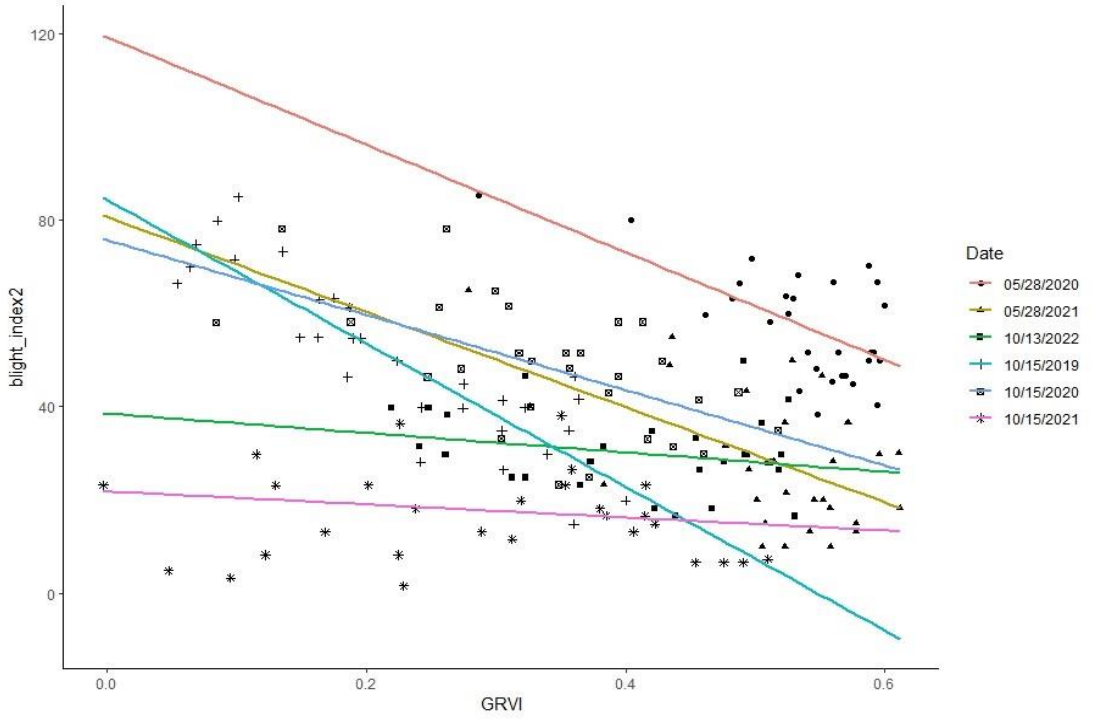

Figure 2. *GRVI and blight index correlations by survey date*

3.2. Flow Direction and Accumulation

Based on the results of the flow direction and flow accumulation model, there was only one model of significance created as an output from the subsequent zonal statistics function using the D8 algorithm and previously created tree canopy polygon layer. This model summary resulted from the flight data collected on 10/15/2021, providing a P-value of 0.005 and r^2 value of 0.23 (Figure 3). While the P-value of 0.005 indicates a fairly large statistical significance, the r^2 value was lower than desired but still

produced an acceptable goodness of fit for this particular model. Based upon these results, the D8 algorithm outperformed both the DINF and MFD for this particular study using the 1 m resolution captured by the sensor. While there could be a multitude of reasons for this, given the relatively low elevation of this site and unlikelihood of significant amounts of overland flow actually occurring at this location, the more simplistic nature of the D8 algorithm may be better suited at capturing theoretical flow paths in low elevation areas or areas without significant changes in elevation as discussed in Jenson and Domingue (1988).

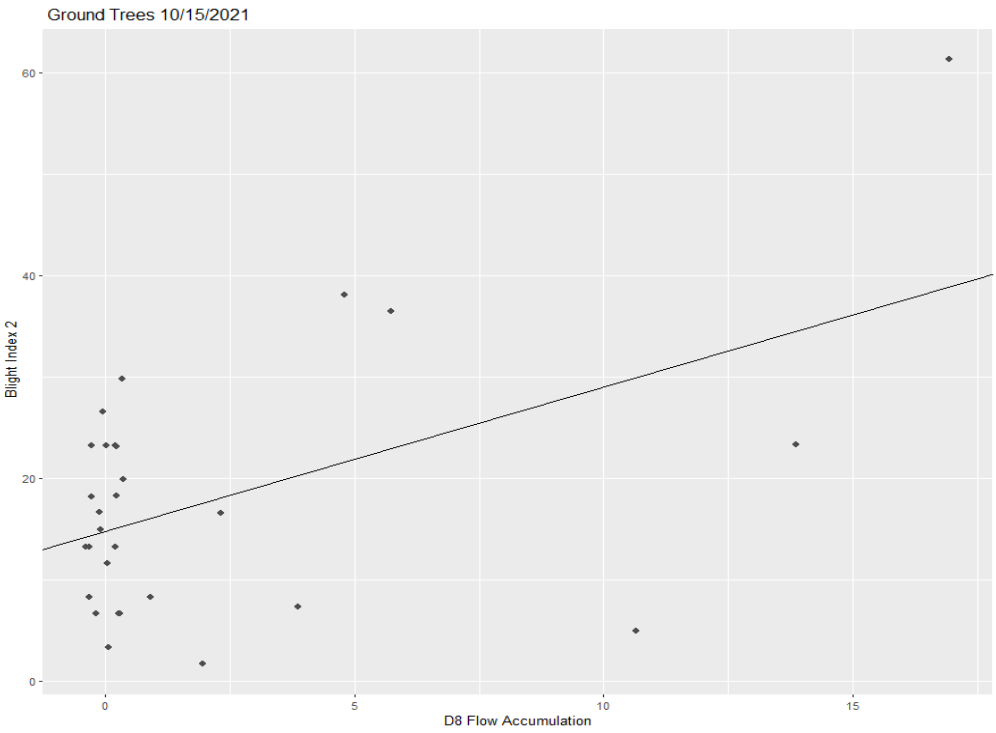

Figure 3. *D8 (Jenson & Dominque 1988) flow accumulation and blight index correlation (P = 0.005, r2 = 0.23).*

4. DISCUSSION

4.1. Vis and Blight Index

Overall, GRVI was found to be the index most correlated with blight presence as determined by our ground survey efforts. It had the strongest correlation for three of the six survey periods and was near the top for a fourth. Conversely, it performed poorly in two of the survey periods (October 2021 and 2002) but no other indices performed strongly during these two years. We considered weather data in trying to determine what factors might have influenced the correlation results. Our sources included the PRISM Climate Group (2022). We accessed mean precipitation and temperature for one year prior each data collection. We found high variation between annual average precipitation and only moderate variation among average temperatures across the survey periods. The strongest correlations between the VIs and blight presence occurred in October 2019 which featured above average precipitation and a below average temperature. All other survey seasons except October 2021 featured below average temperatures. Average annual precipitation was greatest, by far, during the October 2021 season yet this period is characterized by arguably the weakest correlations between the VIs and blight presence. The October 2022 season was also characterized by low correlations between VIs and blight presence but below average precipitation. While there may be a correlation between weather and VI performance in detecting blight, only the October 2019 weather data appear to be associated with positive VI performance.

4.2. (Flow Accumulation): (cite) -> (Bennett & Shaw 2008)

Results of linear regressions produced for each flight using mean flow accumulations from D8 and D infinity methods and blight index as the dependent variable did not demonstrate statistical significance, with the exception of the October 2021 flight and the D8 method. We expected to demonstrate a correlation between flow accumulation as PMLB is thought to spread via water particles (cite). It is

notable that the site experienced more intense drought conditions in October 2021 relative to the other October flights. During periods of drought, trees are more susceptible to disease, and although there may have been less precipitation, trees' susceptibility to pathogens that cause PMLB may have been enhanced. Our temporal observations are limited, but this result may warrant further investigation. Additional variables, that may contribute to spread of foliar diseases include wind direction and potential sheltering from prevailing winds as water droplets may move throughout the site via air turbulence.

Weight rasters, which were not used in this particular model could be applied to flow accumulation to account for differences in precipitation during these time periods. In theory, this additional input could be used to assist in accounting for things such as how much average rain had fallen in an area. This could lead to an output that represented the flow of this rainfall through each cell if it were to become surface runoff as demonstrated by Jenson and Domingue (1988). This additional input could assist in improving the accuracy of the flow accumulation model in other areas depending on terrain conditions. Our study site is relatively small in surface area and contributing area making it unlikely that surface runoff would occur in significant amounts.

5. Conclusion

Our objectives were to explore the use of a multispectral sensor mounted on an UAS for investigating blight spatial-temporal patterns in a Pacific madrone orchard. We examined potential relationships of blight presence with remotely-sensed vegetation health indices. We also assessed potential hydrological vectors for blight patterns. We found that GRVI had the strongest correlation with blight presence across time. Among the several flow accumulation models we tested, only the D8 flow accumulation model (Jenson & Dominque 1988) was statistically significantly related to blight presence. Our methods and results provide continued support for the efficiency of using high resolution mutli-band imagery for investigating blight presence in forested landscapes.

6. Acknowledgements

The authors thank Sean Dose, Weston Hustace, and Sadie Keller for their assistance in conducting fieldwork and manuscript preparation.

References

[1] Agisoft. 2024. Agisoft Metashape User Manual. Available from https://www.agisoft.com/downloads/user-manuals/, accessed November 11, 2024.

[2] Bagheri, N. 2020. Application of aerial remote sensing technology for detection of fire blight infected pear trees. Computers and electronics in agriculture **168**: 105147. doi:10.1016/j.compag.2019.105147.

[3] Barker M.I., Burnett J.D., Haddad T., Hirsch W., Kun Kang D., Pawlak-Kjolhaug K., Wing M.G. 2023. Multi-temporal Pacific madrone leaf blight assessment with unoccupied aircraft systems. Ann. For. Res. 66(1): 171-186, 2023.

[4] Barnes, E., Clarke, T.R., Richards, S.E., Colaizzi, P., Haberland, J., Kostrzewski, M., Waller, P., Choi, C., Riley, E., and Thompson, T.L. 2000. Coincident detection of crop water stress, nitrogen status, and canopy density using ground based multispectral data.

[5] Baston, D., ISciences, L. L. C., & Baston, M. D. 2021. Package 'exactextractr'. R Foundation for Statistical Computing. URL: https://cran. r-project. org.

[6] Bennett, M. and Shaw, D.C. 2008. Diseases and insect pests of Pacific madrone. [Corvallis, Or.] : Oregon State University, Extension Service.

[7] Calderón, R., Navas-Cortés, J.A., Lucena, C., and Zarco-Tejada, P.J. 2013. High-resolution airborne hyperspectral and thermal imagery for early detection of Verticillium wilt of olive using fluorescence, temperature and narrow-band spectral indices. Remote sensing of environment **139**: 231-245. doi:10.1016/j.rse.2013.07.031.

[8] Cao, Q., Miao, Y., Wang, H., Huang, S., Cheng, S., Khosla, R., and Jiang, R. 2013. Non-destructive estimation of rice plant nitrogen status with Crop Circle multispectral active canopy sensor. Field Crops Research **154**: 133-144. doi:https://doi.org/10.1016/j.fcr.2013.08.005.

[9] Chen, J.M. 1996. Evaluation of Vegetation Indices and a Modified Simple Ratio for Boreal Applications. Canadian Journal of Remote Sensing **22**(3): 229-242. doi:10.1080/07038992.1996.10855178.

[10] DeWald, L.E., Elliott, M., Sniezko, R.A., and Chastagner, G.A. Geographic and local variation in Pacific madrone (Arbutus menziesii) leaf blight. *In* Poster session presented at the 6th International Workshop on

the Genetics of Tree-Parasite Interactions: Tree Resistance to Insects and Diseases: Putting Promise into Practice. Mt. Sterling, OH 2018.

[11] Di Nisio, A., Adamo, F., Acciani, G., and Attivissimo, F. 2020. Fast Detection of Olive Trees Affected by Xylella Fastidiosa from UAVs Using Multispectral Imaging. Sensors (Basel, Switzerland) **20**(17): 4915. doi:10.3390/s20174915.

[12] Elliott, M. Diseases of Pacific Madrone. *In* The Decline of Pacific Madrone (Arbutus menziesii Pursh): Current Theory and Research Directions. Seattle, Washington 1999. *Edited by* A.B. Adams. pp. 48-60.

[13] Elliott, M., Edmonds, R., and Mayer, S. 2002. Role of fungal diseases in decline of Pacific madrone. Northwest Science **76**: 293-303.

[14] Elliott, M., Chastagner, G.A., Dermott, G., Kanaskie, A., Sniezko, R.A., and Hamlin, J. Range-wide genetic variability in Pacific madrone (Arbutus menziesii): examining disease resistance, growth, and survival in a common garden study. *In* Sniezko, Richard A.; Yanchuk, Alvin D.; Kliejunas, John T.; Palmieri, Katharine M.; Alexander, Janice M.; Frankel, Susan J., tech. coords. Proceedings of the fourth international workshop on the genetics of host-parasite interactions in forestry: Disease and insect resistance in forest trees. Gen. Tech. Rep. PSW-GTR-240. Albany, CA: Pacific Southwest Research Station, Forest Service, U.S. Department of Agriculture 2012. pp. 295 - 300.

[15] ESRI. 2024. ArcGIS Pro. https://www.esri.com/en-us/arcgis/products/arcgis-pro/overview, accessed November 11, 2024.

[16] Garza, B.N., Ancona, V., Enciso, J., Perotto-Baldivieso, H.L., Kunta, M., and Simpson, C. 2020. Quantifying Citrus Tree Health Using True Color UAV Images. Remote sensing (Basel, Switzerland) **12**(1): 170. doi:10.3390/rs12010170.

[17] Gitelson, A.A., Kaufman, Y.J., and Merzlyak, M.N. 1996. Use of a green channel in remote sensing of global vegetation from EOS-MODIS. Remote sensing of environment **58**(3): 289-298. doi:10.1016/s0034-4257(96)00072-7.

[18] Gitelson, A.A., Viña, A., Ciganda, V., Rundquist, D.C., and Arkebauer, T.J. 2005. Remote estimation of canopy chlorophyll content in crops. Geophysical Research Letters **32**(8): L08403-n/a. doi:10.1029/2005GL022688.

[19] Guimarães, N., Pádua, L., Marques, P., Silva, N., Peres, E., and Sousa, J.J. 2020. Forestry Remote Sensing from Unmanned Aerial Vehicles: A Review Focusing on the Data, Processing and Potentialities. Remote sensing (Basel, Switzerland) **12**(6): 1046. doi:10.3390/rs12061046.

[20] Hijmans, R. J. 2018. raster: Geographic data analysis and modeling. *R package version*, *2*, 8.

[21] Hostens, D.S., Dogwiler, T., Hess, J.W., Pavlowsky, R.T., Bendix, J., and Martin, D.T. 2022. Assessing the Role of sUASSmall unoccupied aerial systems (sUAS) Mission DesignMission designs in the Accuracy of Digital Surface Models Derived from Structure-from-Motion PhotogrammetryPhotogrammetry. *In* sUAS Applications in Geography. *Edited by* K. Konsoer, M. Leitner, and Q. Lewis. Springer International Publishing, Cham. pp. 123-156.

[22] Hunt, E.R., Daughtry, C.S.T., Eitel, J.U.H., and Long, D.S. 2011. Remote Sensing Leaf Chlorophyll Content Using a Visible Band Index. Agronomy journal **103**(4): 1090-1099. doi:10.2134/agronj2010.0395.

[23] Hunt, E.R., Doraiswamy, P.C., McMurtrey, J.E., Daughtry, C.S.T., Perry, E.M., and Akhmedov, B. 2013. A visible band index for remote sensing leaf chlorophyll content at the canopy scale. ITC journal **21**: 103-112. doi:10.1016/j.jag.2012.07.020.

[24] Jenson, S. K. & Dominque, J. O. 1988. Extracting Topographic Structure from Digital Elevation Data for Geographic Information System Analysis. *Photogrammetric Engineering and Remote Sensing*, *54*(11), 1593–1600.

[25] Lucas, J.A. and Dickinson, C.H. 1998. Plant pathology and plant pathogens. 3rd ed. ed. Malden, Mass.: Blackwell Science, Malden, Mass.

[26] Marin, D.B., de Carvalho Alves, M., Pozza, E.A., Belan, L.L., and de Oliveira Freitas, M.L. 2018. Multispectral radiometric monitoring of bacterial blight of coffee. Precision agriculture **20**(5): 959-982. doi:10.1007/s11119-018-09623-9.

[27] Marques, P., Pádua, L., Adão, T., Hruška, J., Peres, E., Sousa, A., and Sousa, J.J. 2019. UAV-Based Automatic Detection and Monitoring of Chestnut Trees. Remote Sensing **11**(7): 855.

[28] Micasense. 2020. Altum - Micasense. Available from https://micasense.com/altum/, accessed November 11, 2024.

[29] Nesbit, P.R. and Hugenholtz, C.H. 2019. Enhancing UAV–SfM 3D Model Accuracy in High-Relief Landscapes by Incorporating Oblique Images. Remote Sensing **11**(3): 239.

[30] The Oregon Department of Geology and Mineral Industries (DOGAMI) Oregon Lidar Consortium. 2024. https://www.oregon.gov/dogami/lidar/pages/index.aspx, accessed November 11, 2024.

[31] PRISM Climate Group, Oregon State University. 2022. Available from https://prism.oregonstate.edu, data created 2022, accessed 6 Nov 2022.

[32] Qin, C., Zhu, A. -X., Pei, T., Li, B., Zhou, C., & Yang, L. 2007. An adaptive approach to selecting a flow-partition exponent for a multiple-flow-direction algorithm. International Journal of Geographical Information Science, 21(4), 443–458. https://doi.org/10.1080/13658810601073240

[33] R Core Team. 2021. R: A Language and Environment for Statistical Computing. Vienna, Austria.

[34] Reeves, S.L. 2007. Arbutus menziesii. Available from https://www.fs.fed.us/database/feis/plants/tree/arbmen/all.html [accessed January 11 2022].

[35] Rouse, J.W., Jr., Haas, R.H., Schell, J.A., and Deering, D.W. 1974. Monitoring Vegetation Systems in the Great Plains with Erts. p. 309.

[36] Sampson, A.W. and Jesperson, B., S. 1963. California range brushlands and browse plants. Berkeley: Division of Agricultural Sciences, University of California, Berkeley. pp. 127.

[37] Sandino, J., Pegg, G., Gonzalez, F., and Smith, G. 2018. Aerial Mapping of Forests Affected by Pathogens Using UAVs, Hyperspectral Sensors, and Artificial Intelligence. Sensors **18**(4). doi:10.3390/s18040944.

[38] Tarboton, D. G. 1997. A new method for the determination of flow directions and upslope areas in grid digital elevation models. *Water Resources Research*, *33*(2), 309–319. https://doi.org/10.1029/96WR03137

[39] Tucker, C.J. 1979. Red and photographic infrared linear combinations for monitoring vegetation. Remote sensing of environment **8**(2): 127-150. doi:10.1016/0034-4257(79)90013-0.

[40] USDA. 2006. Pacific madrone - Plant Guide. The PLANTS Database (http://plants.usda.gov). National Plant Data Team, Greensboro, NC 27401-4901 USA.

[41] Wing, M.G. 2019. Unmanned aircraft systems for remote sensing of vegetation vigor. JOJ Hortic Arboric **2**(4).

[42] Zarco-Tejada, P.J., González-Dugo, V., and Berni, J.A.J. 2012. Fluorescence, temperature and narrow-band indices acquired from a UAV platform for water stress detection using a micro-hyperspectral imager and a thermal camera. Remote sensing of environment **117**: 322-337. doi:10.1016/j.rse.2011.10.007.

Citation: *Michael Wing et al. Applying Unoccupied Aircraft System Multispectral Remote Sensing to Examine Blight in a Pacific Madrone Orchard. International Journal of Forestry and Horticulture (IJFH. 2024; 10(1):20-30. DOI: https://doi.org/10.20431/ 2454-9487.1001004*